Black-box models for Bacterial-Cellulose-based sensors

Luca Patanè, Francesca Sapuppo, Sara Sadat Hosseini, Riccardo Caponetto, Maria Gabriella Xibilia

***Abstract*— In this work, black-box modeling techniques are applied to Bacterial Cellulose-based sensors to characterize their dynamic behavior. Several classes of linear and nonlinear models, including Finite Impulse Response, AutoRegressive with eXogenous Input, Nonlinear Finite Impulse Response, Nonlinear AutoRegressive with eXogenous Input, and Long Short-Term Memory networks, are developed and compared. The performance of each model is evaluated based on a one-step-ahead prediction and a ∞-step-ahead simulation using standard performance metrics such as Root Mean Square Error, Mean Absolute Error and the coefficient of determination. The results show the strengths and limitations of the different modeling approaches in capturing the dynamics of BC-based transducers. The ARX model showed the best results for the prediction in one step, but poor results were obtained when the prediction was considered in ∞ steps. The NFIR model is instead the best choice for long-term prediction.**

I. INTRODUCTION

Polymers have played a crucial role in the development of sensors and electronic devices due to their versatility. Among them, ionic electroactive polymers (IEAPs) have attracted much attention due to their ability to enable scalable, lightweight and flexible motion-sensing systems. However, a major drawback of these materials is their limited environmental sustainability. To address this problem, biologically produced polymers have emerged as a promising alternative. They offer the potential to develop environmentally friendly electronic devices, while retaining the advantageous properties of conventional polymers. Among biopolymers, cellulose has been widely studied for applications in electronics and transducers. Bacterial Cellulose (BC) in particular, has gained interest as a more sustainable and higher-performing alternative to plant-derived cellulose, making it a compelling candidate for next-generation sensor technologies.

BC is a biopolymer synthesized by bacteria such as *Gluconacetobacter hansenii* and *Acetobacter xylinum*. Unlike plant-derived cellulose, BC is highly pure and has a fibrillar nanoscale structure that provides remarkable mechanical strength, flexibility and biocompatibility [1]. Due to these properties, BC has been explored for applications in bioelectronics, biomedical devices and sensors [2].

BC can be engineered into functional sensors by integrating it with conductive materials and ionic polymers. The manufacturing process usually involves the cultivation of BC-producing bacteria in a nutrient-rich medium, followed by purification and chemical modification, to improve the electrical properties [3], [4].

A common approach is to impregnate BC with ionic liquids such as 1-ethyl-3-methylimidazolium tetrafluoroborate (EMIM-BF4), which facilitates ion mobility and improves electrochemical performance. In addition, BC can be coated with conductive polymers such as poly(3,4-ethylenedioxythiophene)-polystyrene sulfonic acid (PEDOT-PSS) to form flexible electrodes [5]. The resulting BC-based device behaves like an ionic polymer-metal composite (IPMC), in which mechanical deformations lead to charge redistribution and measurable electrical signals [6].

The transduction mechanism in BC sensors is influenced by factors such as humidity, ion mobility and mechanical stress. The high porosity and hydrophilic nature of BC enable efficient ion transport, making it an ideal candidate for humidity and pressure sensing applications [7]. Despite these advantages, the challenge is to optimize fabrication techniques to ensure consistency, reproducibility and increased sensitivity of BC-based sensors.

BC-based sensors work as mechano-electrical transducers that can convert mechanical stimuli into electrical signals. These sensors have demonstrated their potential in areas such as environmental monitoring, healthcare and flexible electronics [8]. However, despite their promising applications, BC sensors pose significant modeling challenges due to the complex interactions between mechanical deformation, ion migration and electrical conductivity [9].

Various modeling approaches have been explored to describe the behavior of BC-based sensors [10]. White-box models based on first-principles and multiphysics simulations provide detailed insights but require extensive parameterization and computational resources [3]. Grey-box models attempt to simplify the representation by incorporating empirical data while maintaining a certain degree of interpretability [5]. Black box models, which can utilize machine learning techniques, are a viable alternative that allows for data-driven approximations of the sensor's response [6].

There are only preliminary models for BC-based sensors in the literature [11], [12]. The similarities of BC with other IEAPs could be used to develop models for BC-based transducers. Different classes of models for IEAPs are proposed in the literature: Black box models with neural networks [13], gray box models [14], [15] including fractional order systems [16], [17] and white box models based on computational fluid dynamics (CFD) and finite element methods (FEM) in multiphysics domains [18], [19] are some examples. White Box models rely on a detailed

Luca Patanè, Francesca Sapuppo, Riccardo Caponetto, Maria Gabriella Xibilia are with the Department of Engineering, University of Messina, 98166 Messina, Italy; Sara Sadat Hosseini is with the DIEEI, University of Catania, 95100 Catania, Italy; lpatane@unime.it

This work was funded by European Union - Next Generation EU, Missione 4 Componente 1 CUP J53D23003460006 Green SENSing systems based on Bacterial Cellulose (SENS-BC).

understanding of the system's governing physics, providing insights into both spatial and temporal dynamics. While it ensures high interpretability and accuracy, its computational complexity limits its efficiency for fast simulations, making it less practical for real-time applications. Grey-box model accuracy depends on the quality of prior knowledge and available data, limiting generalizability in highly nonlinear or poorly understood systems.

In this paper, experimental measurements performed on samples of BC-based sensors are used to derive dynamic black-box models. Several classes of models are used and compared, both regarding one- step-ahead prediction and ∞-step-ahead simulation.

II. BLACK-BOX MODELS

Among the different black box identification techniques, both linear and nonlinear solutions previously adopted in modelling composite materials [20], [21] are considered in this paper. In particular, two linear models were used: Finite Impulse Response (FIR) and AutoRegressive with eXogenous input (ARX). Nonlinear models were also considered to assess the presence of nonlinear relationships in the system under study: Nonlinear AutoRegressive with eXogenous input (NARX) and Nonlinear Finite Impulse Response (NFIR). A deep learning model based on Long Short-Term Memory (LSTM) was also included in the analysis to evaluate the performance when recurrent networks are considered.

A. Finite Impulse Response

An FIR model is a linear filter used in signal processing and control systems. It processes input signals using a finite number of past inputs without feedback, which makes it inherently stable [22].

$$y(k) = \sum_{i=1}^{n_b} b_i u(k-i) \tag{1}$$

where $y(k)$ is the output, $u(k)$ the input and b_i the coefficients of the FIR filter. This model is widely used for long-term prediction because it does not require past samples of the output variable.

B. AutoRegressive with eXogenous input

The ARX model is a parametric model used for system identification, incorporating both autoregressive (AR) and exogenous (X) inputs. It assumes a linear relationship between input and output signals with an additional white noise term [23].

$$y(k) + \sum_{i=1}^{n_a} a_i y(k-i) = \sum_{j=1}^{n_b} b_j u(k-j) + e(k) \tag{2}$$

where n_a and n_b are the number of past output and input terms respectively and $e(k)$ is the noise term.

C. Nonlinear Finite Impulse Response

An NFIR model extends the FIR model by including a non-linear function to map past inputs to the current output. This model is useful for capturing complex system dynamics [24].

$$y(k) = f(u(k-1), u(k-2), \ldots, u(k-n_b)) \tag{3}$$

where $f(\cdot)$ is a non-linear function that is applied to past inputs.

D. Nonlinear AutoRegressive with eXogenous Input

A NARX model generalizes the ARX model by incorporating nonlinearities in the relationship between the predicted output and past values of both inputs and outputs. It is often used in system identification and time series prediction [25].

$$y(k) = f(y(k-1), \ldots, y(k-n_a), u(k-1), \ldots, u(k-n_b)) + e(k) \tag{4}$$

where $f(\cdot)$ is a non-linear function. NARX model can be estimated using neural networks to model the nonlinear function. Tapped-delay lines for both input and output variables are used as input for the neural network.

E. Long Short-Term Memory

LSTMs are a type of recurrent neural network that can capture long-term dependencies using gating mechanisms. They are particularly effective for time series prediction and sequence learning tasks [26].

$$f_t = \sigma(W_f x_t + U_f h_{t-1} + b_f) \tag{5}$$
$$i_t = \sigma(W_i x_t + U_i h_{t-1} + b_i) \tag{6}$$
$$\tilde{c}_t = \tanh(W_c x_t + U_c h_{t-1} + b_c) \tag{7}$$
$$c_t = f_t \odot c_{t-1} + i_t \odot \tilde{c}_t \tag{8}$$
$$o_t = \sigma(W_o x_t + U_o h_{t-1} + b_o) \tag{9}$$
$$h_t = o_t \odot \tanh(c_t) \tag{10}$$

where x_t is the input, h_t is the hidden state, c_t is the cell state and $\sigma(\cdot)$ and $\tanh(\cdot)$ are activation functions.

F. Performance indicators

To evaluate the accuracy of the models, the following performance indicators are used:

1) Root Mean Square Error (RMSE): The RMSE measures the standard deviation of the residuals (prediction error). It is defined as:

$$RMSE = \sqrt{\frac{1}{n}\sum_{i=1}^{n}(y_i - \hat{y}_i)^2} \tag{11}$$

where y_i stands for the actual values, $\hat{y}_i$ for the predicted values and n for the number of observations. Lower RMSE values indicate better model performance.

TABLE I: Geometrical parameters.

Parameter description	Value	Unit
Total length, L	4	cm
Base region length, L_B	1.5	cm
Total width, W	1	cm
Thickness of BC, T_{BC}	320	um
Thickness of PEDOT, T_{PSS}	25	um
Distance between magnets and base, L_M	3.7	cm
Distance between laser reading point and base, L_L	3.2	cm

TABLE II: Mechanical Parameters.

Parameter description	Value	Unit
Young modulus of BC-PEDOT compound, E_{BC}	1.64	GPa
Poisson ratio of BC, ν_{BC}	0.01	-
Poisson ratio of PEDOT, ν_{PSS}	0.435	-
Mass density of BC, ρ_{BC}	0.904	g/cm^3
Mass density of PEDOT, ρ_{PSS}	1.28	g/cm^3

2) Mean Absolute Error (MAE): The MAE calculates the average absolute difference between the actual and predicted values. It is given by:

$$MAE = \frac{1}{n}\sum_{i=1}^{n}|y_i - \hat{y}_i| \tag{12}$$

MAE is an intuitive measure of prediction accuracy, with lower values indicating better model performance.

3) Coefficient of Determination (R^2): The R^2 value indicates how well the model explains the variance in the data. It is defined as:

$$R^2 = 1 - \frac{\sum_{i=1}^{n}(y_i - \hat{y}_i)^2}{\sum_{i=1}^{n}(y_i - \bar{y})^2} \tag{13}$$

where $\bar{y}$ is the mean value of the actual output. A value close to 1 indicates a good fit of the model, while a value close to 0 indicates poor predictive performance.

III. EXPERIMENTAL SETUP AND MEASUREMENTS

Measurements have been acquired using a BC device impregnated with EMIM-BF4 as ionic liquid. The geometrical, mechanical electrical and electro-chemical parameters are described in Table I, II, III, IV.

The experimental setup was developed to investigate the mechanical and electrical properties of BC-based composite transducers arranged in a cantilever configuration. This setup allowed controlled mechanical vibrations to be applied to the transducer and its electrical response to be recorded simultaneously.

The transducer was securely attached at one end, called the base clamp, while the free end was fitted with two 2 mm diameter magnets attached to the tip of the BC-based sensor. These magnets were used to generate controlled vibrations via an electromagnetic actuator. The actuator caused the tip of the BC sensor to move by interacting with the magnets, allowing precise control of the vibration amplitude and frequency.

To track the mechanical behavior of the transducer, a laser displacement sensor (BAUMER OADM 12I6460 / S35A)

TABLE III: Chemical parameters.

Parameter description	Value	Unit
Initial ion concentration, C_0	740.88	mol/m^3
Cation diffusion constant, D_{cat}	4×10^{-10}	m^2/s
Anion diffusion constant, D_{an}	4.4×10^{-10}	m^2/s
Cation molar volume, $D_{v_{cat}}$	1.15×10^{-4}	m^3/mol
Anion molar volume, $D_{v_{an}}$	3.85×10^{-5}	m^3/mol
Cation charge number, Z_{cat}	1	-
Anion charge number, Z_{an}	-1	-
Temperature, T	298.15	K
Cation mobility, μ_{cat}	$D_{cat}/(R \cdot T)$	s·mol/kg
Anion mobility, μ_{an}	$D_{an}/(R \cdot T)$	s·mol/kg

TABLE IV: Electrical parameters.

Parameter description	Value	Unit
Electrical conductivity of PEDOT, σ_{PSS}	10	S/cm
Effective absolute dielectric permittivity of BC-PEDOT compound, ϵ	7.8×10^{-7}	F/m

was considered. The laser monitored the deflection of the free end of the transducer, allowing accurate measurement of the mechanical deformation. This deformation was quantified by comparing the deflection at the base clamp with the deflection measured by the laser at the tip of the transducer. This experimental setup provided a reliable platform for evaluating the performance of BC-based transducers by correlating the mechanical vibrations with their electrical outputs, ensuring consistent and accurate measurements. The electrical response of the transducer, in particular the open circuit voltage, was measured directly using a digital oscilloscope. The oscilloscope recorded both the voltage signals from the transducer and the output signals from the laser displacement sensors, enabling a comprehensive analysis of both the electrical and mechanical behavior of the transducer.

A schematic representation of the experimental setup can be found in Fig. 1

The data set used for the following analysis was acquired by applying a frequency sweep signal to the electromagnetic actuator in a range between 2 and 60 Hz. The magnets located near the BC tip are either attracted or repelled, resulting in mechanical stimulation of the device, which has a cantilever configuration. The measurements were performed for $60s$, with an acquisition frequency of $2kHz$. The time evolution of the BC input displacement detected by the laser and the output voltage signal measured at the Pedot electrodes are shown in Fig. 2. The different amplitudes shown by the displacement signal are due to the presence of a mechanical resonance, due to the cantilever configuration of the device, which occurs when the excitation frequency is between 50 and 60 Hz.

The output signal was filtered with a low-pass filter with a cut-off frequency of 60 Hz, as shown in Fig. 3. The available dataset was downsampled according to the Shannon criteria by reducing the sampling frequency to 500Hz.

The dataset was then divided into training, validation (80%) and test (20%) to account for the relevant trends in

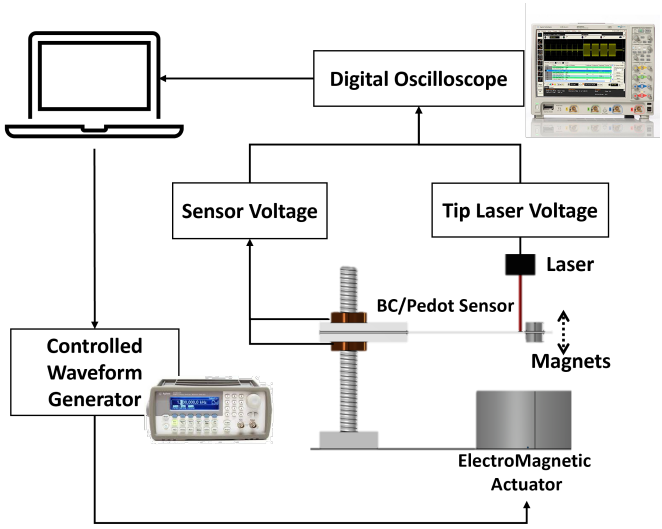

Fig. 1: Experimental setup of the acquisition system.

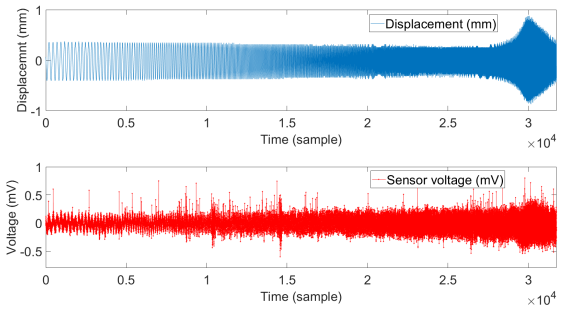

Fig. 2: Time evolution of the tip displacement of the BC (input variable) and voltage acquired between the BC/pedot surfaces (output variable). The sampling frequency used for the modelling phase is 500 Hz.

each subset. The z-score normalization was also applied.

IV. RESULTS

The experimental results show the effectiveness of black-box models in the characterization of BC-based sensors. The FIR model is the simplest solution due to its linearity and the absence of output regressors. This makes it possible to perform simulations without measuring the past output values. Following a trial-and-error procedure guided by the cross-correlation analysis between the output and input variables, n_b=20 input regressors were used.

However, the performance achieved, which is reported in Tab. V, shows that the results are not satisfactory. Specifically, the FIR model achieves an R^2=0.51 and an RMSE=0.88 on the test dataset. The regression plot for the FIR model evaluated with the test dataset is shown in Fig. 4.

To improve the performance of the model, an ARX structure with n_a=10 and n_b=5 was considered. The ARX model exhibits significant improvements in one-step-ahead predictions and achieves an R^2=0.98 for the test dataset. The ∞-step-ahead prediction, on the other hand, is not satisfactory as the R^2 deteriorates to 0.47 and the RMSE increases from 0.12 to 0.92. The regression plot for the ARX

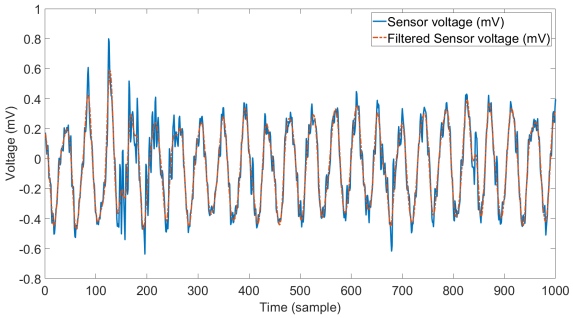

Fig. 3: Output data and corresponding filtered version.

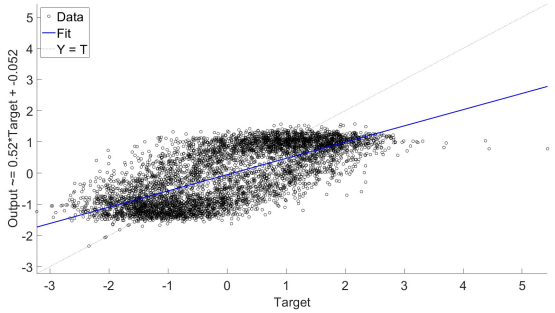

Fig. 4: Regression plot of the FIR model for the test set

model, which was evaluated on the test set, is shown in Fig. 5, where both the 1-step-ahead and the ∞-step-ahead predictions are shown.

The NFIR model was implemented using the same number of regressors of FIR ($n_b = 20$) and considering a multilayer perceptron (MLP) with sigmoidal activation functions. The best results were obtained with a single hidden layer of 10 neurons. As shown in Tab. V, a significant improvement was achieved over both the FIR and ARX models and an R^2=0.77 for the ∞- step-ahead prediction was achieved. This is also illustrated by the regression plot in Fig. 6.

Similarly, a NARX model based on an MLP with a single hidden layer of 10 neurons, $n_a = 5$ and $n_b = 3$ was considered which achieved an improvement in ∞-step-ahead prediction over the ARX model with an R^2=0.69. However, the performance achieved with the NFIR is still better than that of the NARX model. The regression plot for the NARX model evaluated on the test set is shown in Fig. 7, where both the 1-step-ahead and the ∞-step-ahead predictions are shown.

An LSTM model was also used for comparison. Good performance is achieved for the 1-step-ahead prediction reaching an R^2=0.97, while poorer results are obtained in the ∞-step-ahead prediction in both the training (R^2=0.53) and test datasets (R^2=0.46). The regression plot for the LSTM model evaluated on the test set is reported in Fig. 8 where both the 1-step-ahead and the ∞-step-ahead predictions are shown.

The behaviour of the two best models, i.e. NFIR and NARX, is reported in Figures 9, 10 and 11, which show the comparison between the actual and predicted results in

TABLE V: Performance of the models in training and test for the 1-step and ∞-step-ahead prediction.

	1-step Prediction						∞-step Prediction					
	Train			Test			Train			Test		
	RMSE	**MAE**	R^2	**RMSE**	**MAE**	R^2	**RMSE**	**MAE**	R^2	**RMSE**	**MAE**	R^2
FIR	0.86	0.67	0.49	0.88	0.72	0.51	0.86	0.67	0.49	0.88	0.72	0.51
ARX	**0.15**	**0.10**	**0.98**	**0.12**	**0.09**	**0.99**	0.90	0.72	0.43	0.92	0.76	0.47
NFIR	0.61	0.48	0.74	0.63	0.50	0.77	**0.61**	**0.48**	**0.74**	**0.63**	**0.50**	**0.77**
NARX	0.17	0.13	**0.98**	0.16	0.11	0.95	0.77	0.59	0.50	0.77	0.62	0.69
LSTM	0.17	0.12	0.95	0.18	0.14	0.97	0.70	0.57	0.53	0.88	0.72	0.46

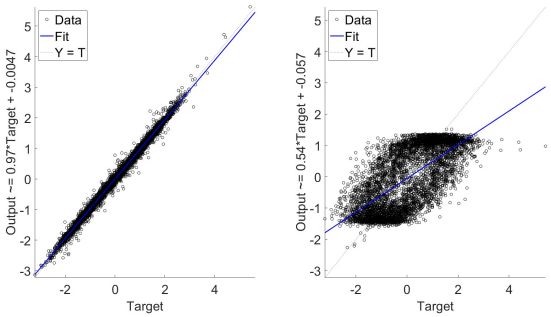

Fig. 5: Regression plot of the ARX model for the test set: 1-step-ahead prediction (left panel), ∞-step-ahead prediction (right panel).

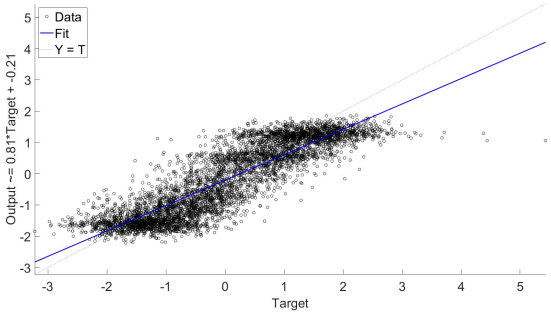

Fig. 6: Regression plot of the NFIR model for the test set.

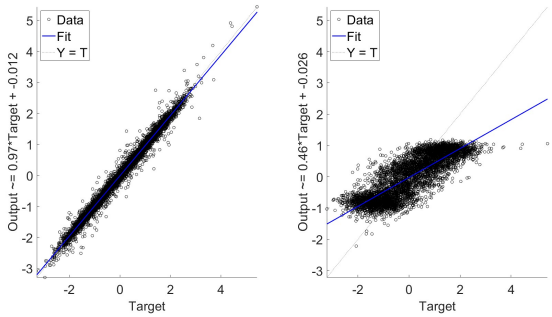

Fig. 7: Regression plot of the NARX model for the test set: 1-step-ahead prediction (left panel), ∞-step-ahead prediction (right panel).

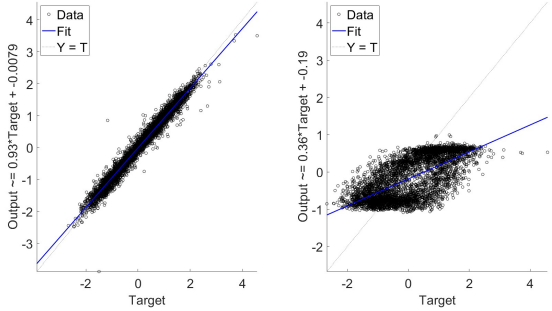

Fig. 8: Regression plot of the LSTM model for the test set: 1-step-ahead prediction (left panel), ∞-step-ahead prediction (right panel) .

the training and two subsets of the test datasets.

The two test subsets were selected to show the behaviour of the models at different excitation frequencies. In particular, the NFIR shows similar performance to the NARX at low input frequencies, while the NARX shows better performance at high frequencies when the 1-step-ahead prediction is considered. For ∞-step prediction, the performance of NARX degrades significantly for both training and test data in the whole frequency range (see Fig. 11).

The NFIR model has proven to be the best-performing model and shows superior long-term predictive ability relevant for simulation and control purposes. Further experimental campaigns are needed to evaluate the generalization capability of the model.

V. CONCLUSION

This study presents a comparative analysis of black-box models for BC-based sensors. The results show that FIR and ARX models provide a basic understanding, while nonlinear models such as NFIR, NARX and LSTM improve the prediction accuracy. In particular, the proposed ARX model is able to achieve high performance in 1-step prediction (R^2=0.99, RMSE=0.12, MAE=0.09), but fails in predicting the output value when long-term prediction is required (R^2=0.47, RMSE=0.92, MAE=0.76). On the other hand, the NFIR models perform equally well in short and long-term prediction due to the lack of output regressors and achieve the best performance among the models considered (R^2=0.77, RMSE=0.63, MAE=0.50).

Future work will focus on refining the models in further experiments to verify the generalization capabilities of the model. In addition, the possibility of including external conditions such as humidity and temperature, the size of the sensor and the type of ionic liquids among the inputs is under investigation.

VI. ACKNOWLEDGEMENTS

The authors acknowledge the PRIN research unit of the University of Catania coordinated by Prof. Salvatore Graziani for the BC measurements used in this work.

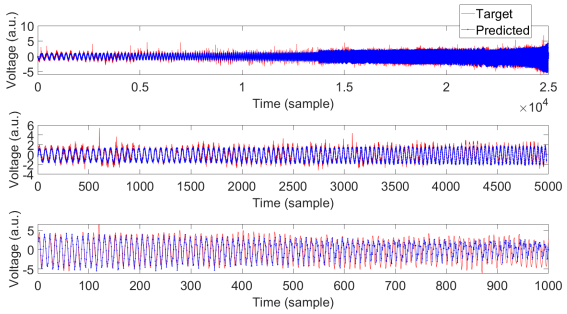

Fig. 9: Comparison between the target and predicted output signals for the NFIR model: training data (first panel), test data (second and third panels).

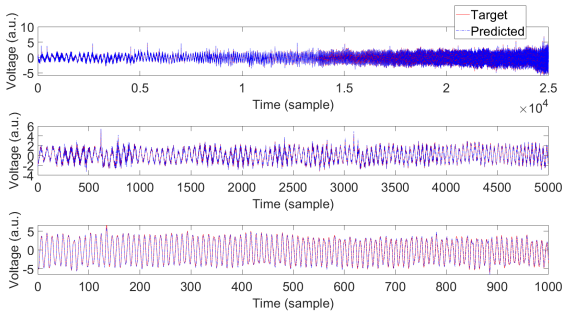

Fig. 10: Comparison between the target and predicted output signals for the NARX model with a 1-step-ahead prediction: training data (first panel), test data (second and third panels).

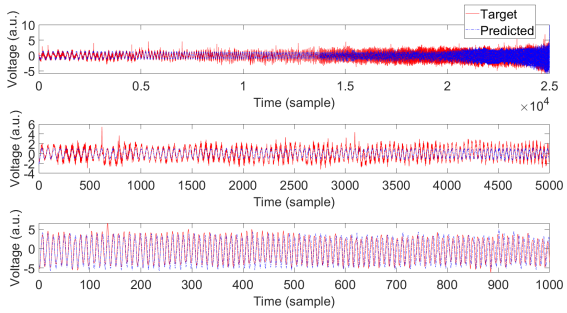

Fig. 11: Comparison between the target and predicted output signals for the NARX model with a ∞-step-ahead prediction: training data (first panel), test data (second and third panels).

REFERENCES

[1] J. D. Yuen, L. C. Shriver-Lake, S. A. Walper, D. Zabetakis, J. C. Breger, and D. A. Stenger, "Microbial nanocellulose printed circuit boards for medical sensing," *Sensors*, vol. 20, no. 7, p. 2047, 2020.

[2] J. Huang, M. Zhao, Y. Hao, and Q. Wei, "Recent advances in functional bacterial cellulose for wearable physical sensing applications," *Advanced Materials Technologies*, vol. 7, no. 1, p. 2100617, 2022.

[3] C. Trigona, S. Cerruto, S. Graziani, G. D. Pasquale, and A. Pollicino, "Towards environmentally friendly accelerometers based on bacterial cellulose," *Applied Sciences*, vol. 11, no. 17, p. 7903, 2021.

[4] J. Wang, J. Tavakoli, and Y. Tang, "Bacterial cellulose production, properties and applications with different culture methods – a review," *Carbohydrate Polymers*, vol. 219, pp. 63–76, 2019.

[5] R. Caponetto, G. D. Pasquale, S. Graziani, A. Pollicino, F. Sapuppo, and C. Trigona, "Modeling of bacterial cellulose-based composite," *Electronics*, vol. 12, no. 21, p. 4530, 2023.

[6] L. Yang, Y. Yang, and H. Wang, "Modeling and control of ionic polymer metal composite actuators: A review," *European Polymer Journal*, vol. 186, p. 111821, 2023.

[7] G. D. Pasquale, S. Graziani, A. Licciulli, R. Nisi, A. Pollicino, and C. Trigona, "Geometrical analysis of a bacterial cellulose-based sensing element," pp. 225–228, 2019.

[8] Y.-H. Wang, P. Song, X. Li, C. Ru, G. Ferrari, P. Balasubramanian, M. Amabili, Y. Sun, and X. Liu, "A paper-based piezoelectric accelerometer," *Micromachines*, vol. 9, no. 1, p. 19, 2018.

[9] G. D. Pasquale, S. Graziani, A. Pollicino, and C. Trigona, "Performance characterization of a biodegradable deformation sensor based on bacterial cellulose," *IEEE Transactions on Instrumentation and Measurement*, vol. 69, no. 5, pp. 2561–2569, 2020.

[10] L. Patanè, F. Sapuppo, M. Calapristi, G. Di Pasquale, S. Graziani, A. Pollicino, C. Trigona, and M. G. Xibilia, "A multiphysics framework for bacterial cellulose sensor modeling," in *2024 IEEE International Conference on Metrology for eXtended Reality, Artificial Intelligence and Neural Engineering (MetroXRAINE)*, 2024, pp. 612–617.

[11] C. Trigona, S. Cerruto, S. Graziani, G. Di Pasquale, and A. Pollicino, "Towards environmentally friendly accelerometers based on bacterial cellulose," *Applied Sciences*, vol. 11, no. 17, 2021. [Online]. Available: https://www.mdpi.com/2076-3417/11/17/7903

[12] R. Caponetto, G. Di Pasquale, S. Graziani, A. Pollicino, F. Sapuppo, and C. Trigona, "Modeling of bacterial cellulose-based composite," *Electronics*, vol. 12, no. 21, 2023. [Online]. Available: https://www.mdpi.com/2079-9292/12/21/4530

[13] L. Yang, Y. Yang, and H. Wang, "Modeling and control of ionic polymer metal composite actuators: A review," *European Polymer Journal*, vol. 186, p. 111821, 2023.

[14] M. Vahabi, E. Mehdizadeh, M. Kabganian, and F. Barazandeh, "Experimental identification of ipmc actuator parameters through incorporation of linear and nonlinear least squares methods," *Sensors and Actuators A: Physical*, vol. 168, no. 1, pp. 140–148, 2011.

[15] A. Punning, U. Johanson, M. Anton, A. Aabloo, and M. Kruusmaa, "A distributed model of ionomeric polymer metal composite," *Journal of Intelligent Material Systems and Structures*, vol. 20, no. 14, pp. 1711–1724, 2009.

[16] R. Caponetto, S. Graziani, F. Sapuppo, and V. Tomasello, "An Enhanced Fractional Order Model of Ionic Polymer-Metal Composites Actuator," *Advances in Mathematical Physics*, vol. 2013, pp. 1–6, August 2013.

[17] R. Caponetto, S. Graziani, F. Pappalardo, and F. Sapuppo, "Identification of ipmc nonlinear model via single and multi-objective optimization algorithms," *ISA Transactions*, vol. 53, no. 2, pp. 481–488, 2014.

[18] R. Caponetto, V. De Luca, G. Di Pasquale, S. Graziani, F. Sapuppo, and E. Umana, "A multiphysics frequency-dependent model of an $\mathrm{ip}^2\mathrm{c}$ actuator," *IEEE Transactions on Instrumentation and Measurement*, vol. 63, no. 5, pp. 1347–1355, 2014.

[19] Q. He, D. Vokoun, T. Stalbaum, K. J. Kim, A. I. Fedorchenko, X. Zhou, M. Yu, and Z. Dai, "Mechanoelectric transduction of ionic polymer-graphene composite sensor with ionic liquid as electrolyte," *Sensors and Actuators A: Physical*, vol. 286, pp. 68–77, 2019.

[20] B. Andò, S. Graziani, and M. G. Xibilia, "Low-order nonlinear finite-impulse response soft sensors for ionic electroactive actuators based on deep learning," *IEEE Transactions on Instrumentation and Measurement*, vol. 68, no. 5, pp. 1637–1646, 2019.

[21] S. Graziani, E. Umana, M. Xibilia, and V. De Luca, "Multi-input identification of ip2c actuators," in *2013 IEEE International Instrumentation and Measurement Technology Conference (I2MTC)*, 2013, pp. 1147–1151.

[22] A. V. Oppenheim and R. W. Schafer, *Discrete-Time Signal Processing*, 2nd ed. Prentice Hall, 1999.

[23] L. Ljung, *System Identification: Theory for the User*, 2nd ed. Prentice Hall, 1999.

[24] S. A. Billings, *Nonlinear System Identification: NARMAX Methods in the Time, Frequency, and Spatio-Temporal Domains*. Wiley, 2013.

[25] K. S. Narendra and K. Parthasarathy, "Identification and control of dynamical systems using neural networks," *IEEE Transactions on Neural Networks*, vol. 1, no. 1, pp. 4–27, 1990.

[26] S. Hochreiter and J. Schmidhuber, "Long short-term memory," *Neural Computation*, vol. 9, no. 8, pp. 1735–1780, 1997.